RSC Advances

PAPER

View Article Online
View Journal | View Issue

Cite this: *RSC Adv.*, 2025, **15**, 33708

First-principles investigation of lead-free Rb_3SbX_6 (X = F, Cl, Br, I) mixed-halide double perovskites promising for photovoltaics and scintillation

Muhammad Awais Jehangir,[a] Muhammad Yar Khan,*[b] Muhammad Noman,[a] It Ee Lee,*[cd] Qamar Wali,[cd] Tariq Usman,[b] Yang Mu[b] and Abdullah Al Souwaileh[e]

In this work, density functional theory (DFT) calculations were performed to systematically explore the structural, mechanical, electronic, optical, light yield and thermodynamic properties of a series of environmentally benign, lead-free mixed-halide double perovskites with the general formula Rb_3SbX_6 (X = F, Cl, Br, I). The optimized lattice constants were found to increase from 9.61 Å for Rb_3SbF_6 to 13.01 Å for Rb_3SbI_6. Electronic band structures were obtained using the Tran–Blaha modified Becke–Johnson (TB-mBJ) exchange–correlation functional, revealing a decreasing band gap trend from 5.477 eV (F) to 2.851 eV (I), in accordance with the increasing ionic radius of the halide anions. Density of states (DOS) analysis highlighted the specific orbital contributions to the valence and conduction bands. Optical properties, including the complex dielectric function $\varepsilon(\omega)$, absorption coefficient $\alpha(\omega)$, reflectivity $R(\omega)$, and refractive index $n(\omega)$, were evaluated, demonstrating strong optical responses across the series. Notably, the estimated ideal light yield for Rb_3SbI_6 indicates its potential for scintillation applications. Thermodynamic stability was assessed through temperature-dependent calculations of the Gibbs free energy, unit cell volume, entropy (S, J mol^{-1} K^{-1}), and bulk modulus (B, GPa). The results consistently exhibit negative Gibbs free energies, thermal expansion with increasing temperature, rising entropy, and a gradual decrease in bulk modulus, confirming good thermal stability. These findings suggest that Rb_3SbX_6 (X = F, Cl, Br, I) double perovskites are promising candidates for use in radiation detection and optoelectronic devices.

Received 9th July 2025
Accepted 20th August 2025

DOI: 10.1039/d5ra04902d

rsc.li/rsc-advances

1 Introduction

In recent years, perovskite-derived materials have attracted widespread interest within the scientific community due to their remarkable crystal structures and diverse range of functional attributes. These characteristics make them highly suitable for integration into numerous advanced technologies, such as optoelectronic devices, energy storage systems, and radiation detectors. The canonical perovskite lattice, generally expressed by the formula ABX_3, is particularly notable for its excellent light absorption, efficient charge transport properties, and favorable optical behavior. Such advantages have led to its incorporation in applications including photovoltaic cells, light-emitting diodes (LEDs), photodetectors, and scintillation devices. Importantly, the structural and electronic versatility of perovskites can be enhanced through compositional tuning at the A, B, and X sites, allowing for a wide scope of material optimization. Among these, halide-based perovskites where the X-site is occupied by a halogen have emerged as a dynamic and rapidly growing field of study due to their adaptable chemistry and superior optoelectronic performance.[1,2] Kojima *et al.* first introduced an organo-lead halide perovskite as a light-harvesting material in dye-sensitized perovskite solar cells (PSCs), reporting an initial power conversion efficiency (PCE) of approximately 3.8%.[2] Since this initial demonstration, the PCE has steadily improved, exceeding 22% by 2017, approaching the theoretical limit of ~27%.[3] Notably, the highest reported efficiency of 22.1% has been achieved using halide perovskite materials.[4,5] These materials exhibit remarkable photovoltaic performance due to favorable properties such as balanced electron and hole mobilities, long carrier diffusion lengths, low exciton binding energies, high optical absorption coefficients, suitable bandgaps, and defect tolerance. Furthermore, the cost-effective and straightforward solution-based synthesis of halide perovskites enhances their potential as ideal absorber materials for emerging photovoltaic technologies.[6]

Halide perovskites have drawn considerable attention in optoelectronics due to their strong light absorption, long carrier diffusion lengths, and tunable electronic band gaps. However,

[a]*Material Modeling Lab, Department of Physics, Islamia College, Peshawar, Pakistan*
[b]*Department of Physics, Qilu Institute of Technology, 250200, Jinan, Shandong Province, P.R. China. E-mail: hmyarkhan@yahoo.com*
[c]*Faculty of Artificial Intelligence and Engineering, Multimedia University, 63100 Cyberjaya, Malaysia. E-mail: ielee@mmu.edu.my*
[d]*Centre for Smart System and Automation, COE for Robotics and Sensing Technologies, Multimedia University, 63100 Cyberjaya, Malaysia*
[e]*Department of Chemistry, College of Science, King Saud University, Riyadh 11451, Saudi Arabia*

the prevalent reliance on lead-based compositions has led to significant environmental and health concerns, given lead's toxicity and the limited intrinsic stability of these materials.[7–9] In response, researchers have devoted extensive efforts to identifying lead-free alternatives capable of maintaining favorable optoelectronic properties without the associated hazards.[10–12] Single and double halide perovskites are among the most promising candidates in this regard. Within this broad class, the A_3BX_6-type halide double perovskites have emerged as an especially intriguing subgroup. Structurally, these compounds can be seen as vacancy-ordered derivatives of the traditional cubic perovskite lattice, where isolated $[BX_6]$ octahedra are separated by alkali-metal cations. This separation reduces the overall dimensional connectivity compared to the classic three-dimensional ABX_3 frameworks.[7,10,13] Such structural features allow considerable compositional flexibility, making it possible to systematically tailor both the stability and electronic properties through careful selection of the A- and X-site ions. Experimental synthesis and characterization of various A_3BX_6 materials have provided important reference points for theoretical exploration. For instance, Rb_3InCl_6 and Rb_3InBr_6 have been shown to crystallize in the cubic $Fm\bar{3}m$ space group, with isolated InX_6 octahedra and band gaps exceeding 4 eV, making them promising candidates for ultraviolet-transparent dielectric applications and deep-UV optoelectronics.[14,15] Likewise, although $Cs_3Bi_2I_9$ adopts a slightly different $A_3B_2X_9$ stoichiometry, its zero-dimensional or layered motifs are structurally related, and its ~2 eV band gap has made it of interest as a lead-free absorber for photovoltaic applications.[16–18] A key advantage of the A_3BX_6 structural motif lies in its potential for band-gap tuning *via* halide substitution. Across the halide series (F, Cl, Br, I), the band gap systematically decreases, primarily due to increasing halide ionic radii and decreasing electronegativity, which elevate the valence-band maximum.[19–21] This behavior has been demonstrated both experimentally and through density functional theory (DFT) simulations, supporting the rational design of materials optimized for diverse uses from UV photodetectors (F, Cl) to visible-light photovoltaic and scintillation technologies (Br, I). Despite these promising characteristics, the Rb_3SbX_6 (X = F, Cl, Br, I) family remains relatively underexplored. Incorporating Sb(III) at the B-site introduces an ns^2 lone-pair configuration, which can generate local structural distortions and defect-tolerant electronic states properties that may be advantageous for optoelectronic performance.[22,23] Early computational investigations suggest that Rb_3SbX_6 compounds exhibit direct or nearly direct band gaps spanning approximately 2.8 eV to 5.5 eV, indicating their potential suitability for photovoltaic and scintillation applications depending on composition.[24,25] Density Functional Theory (DFT) is a first-principles computational approach that enables the study of ground-state properties of materials by reformulating the many-body electron problem in terms of electron density. Its reliability and efficiency make it particularly suitable for predicting the structural, electronic, optical, and thermodynamic characteristics of emerging materials such as halide-based perovskites. Nonetheless, comprehensive first-principles studies examining their structural stability, electronic band structures, optical absorption properties, and defect behavior are still lacking. Such studies are essential for rigorously assessing their potential as environmentally friendly, lead-free semiconductors for device integration.

In a recent study, M. Y. Khan *et al.* (2025) systematically investigated the structural, elastic, optoelectronic, and thermodynamic properties of the novel ternary halide double perovskites Cs_3SbX_6 (X = F, Cl) using density functional theory (DFT). The optimized lattice parameters were found to be 10.12 Å for Cs_3SbF_6 and 11.89 Å for Cs_3SbCl_6. The electronic band gaps were evaluated using the PBE-GGA functional in combination with the Tran–Blaha modified Becke–Johnson (TB-mBJ) potential, revealing that the fluorinated compound exhibits a larger band gap due to the smaller ionic radius of F^- compared to Cl^-. An inverse correlation between the band gap and lattice constant was observed, indicating that an increase in lattice parameter results in a decrease in band gap energy. Density of states (DOS) analysis provided insight into the electronic contributions to the valence and conduction bands. The calculated maximum light yields under ideal conditions were 106 411.28 ph per MeV for Cs_3SbF_6 and 123 304.56 ph per MeV for Cs_3SbCl_6, highlighting their potential application in scintillation detectors. Additionally, optical properties including the complex dielectric function $\varepsilon(\omega)$, absorption coefficient $\alpha(\omega)$, reflectivity $R(\omega)$, and refractive index $n(\omega)$ were computed to evaluate the optical response of these materials. Thermodynamic parameters such as Gibbs free energy and heat capacity suggest good thermal stability, with negative G values and increasing C_v trends. Overall, the findings indicate that Cs_3SbX_6 (X = F, Cl) are promising candidates for high-energy radiation detection and optoelectronic applications.[25]

This work employs density functional theory (DFT) as a first-principle approach to conduct a detailed examination of the structural, electronic, elastic, thermodynamic, and optical features of Rb_3SbX_6 (X = F, Cl, Br, I) halide double perovskites. By analyzing trends in band gaps, dielectric properties, and electronic transitions, the study aims to deliver critical insights that can guide the development of these lead-free materials for use in next-generation photovoltaic absorber layers and scintillation detection technologies.

2 Method of simulations

Structural calculations were carried out using the full-potential linearized augmented plane wave (FP-LAPW) method implemented in the WIEN2K code. The equilibrium volume was determined by fitting the computed total energies to the Birch–Murnaghan equation of state (BM-EOS), employing the PBEsol parameterization of the generalized gradient approximation (GGA).[26] For precise Brillouin zone sampling during structural relaxation, a 10 × 10 × 10 k-point grid was utilized.

$$E(V) = E_0(V) + \left[\frac{B_0}{B_0'\left(B_0' - 1\right)}\right] \times \left[B_0\left(1 - \frac{V_0}{V}\right) + \left(\frac{V_0}{V}\right)^{B_0'} - 1\right] \quad (1)$$

The muffin-tin radii (RMT, in atomic units) assigned to the constituent atoms were: Rb (2.50), Sb (1.41/2.50), F (0.72), Cl (0.99), Br (1.14), and I (1.33). For the plane-wave cutoff, the condition $R_{MT} \times K_{max} = 8$ was applied, with the maximum angular momentum quantum number l_{max} set to 12, and G_{max} specified as 12. The core–valence separation was maintained by adopting a core-state cutoff energy of −6.0 Ry in the WIEN2k calculations. The self-consistent field (SCF) cycles were converged to thresholds of 0.0001 Ryd for total energy and 0.0001e for charge density. Additionally, structural stability assessments of the target compounds were performed *via* calculation of the Goldschmidt tolerance factor (τ_f), and formation enthalpies (ΔH_F).[27]

$$\tau_F = \frac{R_A + R_X}{\sqrt{2}\left(\frac{R_B + R_{B'}}{2}\right) + R_X} \quad (2)$$

$$\Delta H_F = E_{Rb_3SbX_6} - 2E_{Rb} - E_{Sb} - 6E_{F/Cl/Br/I} \quad (3)$$

The PBEsol-GGA approximation has been employed to accurately capture the essential structural characteristics of the system and its ground-state configuration, despite recognized limitations in predicting optoelectronic properties with high precision. To address this, the TB-mBJ potential was utilized, demonstrating notable effectiveness in yielding reliable estimates of the electronic band gap.[28] The elastic tensor components were computed using the method proposed by Morteza Jamal[29–31] within the WIEN2K computational framework, enabling the identification of both spherical and planar harmonic vibrational modes in the material. Furthermore, a comprehensive investigation of the optical properties was conducted to evaluate the potential suitability of these materials for photonic and optoelectronic applications.[32] A central quantity in describing the optical response of a material is the complex dielectric function, which comprises the real part, $\varepsilon_1(\omega)$, and the imaginary part, $\varepsilon_2(\omega)$. The real component, $\varepsilon_1(\omega)$, governs the material's ability to store and refract light, directly influencing its reflectance and transmittance characteristics. Conversely, the imaginary component, $\varepsilon_2(\omega)$, describes energy absorption and loss mechanisms, thereby defining the material's absorption profile across specific energy ranges. The interdependence between $\varepsilon_1(\omega)$ and $\varepsilon_2(\omega)$ is rigorously established through the Kramers–Kronig relations[33] in eqn (14) and (15).

$$\varepsilon_1(\omega) = 1 + \frac{2}{\pi} P \int_0^\infty \frac{\acute{\omega}\varepsilon_2(\acute{\omega})}{\acute{\omega}^2 - \omega^2} d\acute{\omega} \quad (4)$$

$$\varepsilon_2(\omega) = -\frac{2\omega}{\pi} P \int_0^\infty \frac{\acute{\omega}\varepsilon_1(\acute{\omega})}{\acute{\omega}^2 - \omega^2} d\acute{\omega} \quad (5)$$

$$n(\omega) = \left(\frac{1}{2}\left[\sqrt{\varepsilon_1^2(\omega) + \varepsilon_2^2(\omega)} + \varepsilon_1(\omega)\right]\right)^{\frac{1}{2}} \quad (6)$$

$$k(\omega) = \left(\frac{1}{2}\left[\sqrt{\varepsilon_1^2(\omega) + \varepsilon_2^2(\omega)} - \varepsilon_1(\omega)\right]\right)^{\frac{1}{2}} \quad (7)$$

$$\sigma(\omega) = \sigma_1(\omega) + i\sigma_2(\omega) = -i\frac{\omega}{4\pi}[\varepsilon_1(\omega) + i\varepsilon_2(\omega) - 1] \quad (8)$$

$$\alpha(\omega) = \frac{4\pi k(\omega)}{\lambda} = \frac{2\pi k(\omega)}{c} \quad (9)$$

$$R(\omega) = \frac{\text{Ratio of incident light}}{\text{Ratio of reflected light}} = \left|\frac{(\varepsilon_1(\omega) + i\varepsilon_2(\omega))^{1/2} - 1}{(\varepsilon_1(\omega) + i\varepsilon_2(\omega))^{1/2} + 1}\right|^2 \quad (10)$$

$$L(\omega) = \text{Im}\left(\frac{-1}{\varepsilon(\omega)}\right) = \text{Im}\left[\frac{\varepsilon_2(\omega)}{\varepsilon_1^2(\omega) + i\varepsilon_2^2(\omega)}\right] \quad (11)$$

The wave vector (k) and Cauchy principal value (P) are defined accordingly, where h denotes Planck's constant, ω represents the angular frequency, and M refers to the molar mass. Accurate determination of thermodynamic properties under conditions of elevated temperature and pressure is essential for understanding material behavior, a critical aspect of solid-state research and the design of novel materials. In this study, the quasi-harmonic GIBBS2 algorithm[34] was employed to evaluate the thermal stability of the investigated material. Based on the Debye quasi-harmonic approximation, the GIBBS software expresses the Gibbs non-equilibrium function as $G^*(V; P, T)$.[35]

$$G^*(V: P, T) = E(V) + PV + A_{vib}[\Theta_D{:}T] \quad (12)$$

$$A_{vib}[\Theta_D{:}\ T] = nk_BT\left[\frac{9\Theta_D}{k_BT} + 3\ln f\left(1 - e^{\Theta_D/T}\right) - D\left(\frac{\Theta_D}{T}\right)\right] \quad (13)$$

$$D\left(\frac{\Theta_D}{T}\right) = 3\left(\frac{T}{\Theta_D}\right)^3 \int_0^{\Theta_D} \frac{x^3}{e^x - 1} dx \quad (14)$$

The vibrational term and the Debye integral are shown in the eqn (13) and (14). The Entropy of the system is expressed as,

$$S = nk_B\left[4D\left(\frac{\Theta_D}{T}\right) - 3\ln f\left(1 - e^{\Theta_D/T}\right) - D\left(\frac{\Theta_D}{T}\right)\right] \quad (15)$$

3 Results and discussion

3.1 Structural properties

All calculations were performed based on the crystal structures of the Rb_3SbX_6 (X = F, Cl, Br, I) halides, which crystallize in the cubic face-centered space group $Fm\bar{3}m$ (#225). Structural optimizations were carried out using the generalized gradient approximation (GGA) in the Perdew–Burke–Ernzerhof (PBE) functional to determine the ground-state lattice parameters including the lattice constant a_0 [Å] and the bulk modulus B_0 (GPa), pressure derivative B_0', optimized volume V_0 [a.u]^3, and stable state unit cell energy E_0 [Ry.]. The Birch–Murnaghan equation of state[36] was employed for volume optimization to extract the equilibrium lattice constant a_0 [Å] and the bulk modulus B_0 (GPa), as summarized in Table 1. The atomic arrangements in Rb_3SbX_6 adopt a face-centered cubic (FCC)

Table 1 Structural properties of the Rb_3SbX_6 (X = F, Cl, Br, I) halide DPs

Materials	a_0 [Å]	V_0 [a.u]^3	B_0 [GPa]	$B_0^{'}$	E_0 [Ry.]	τ_F	ΔH_F [eV per atom]	E_{Coh}	ρ [g cm^{-3}]	
Rb_3SbF_6	9.61	1501.74	41.30	5.00	−32035.53	1.0	−2.88	0.28	3.67	This work
Cs_3SbF_6	10.12	1752.33	34.80	5.00	−60 908.54	1.1	−2.64	0.26	4.06	25
Rb_3SbCl_6	11.54	2594.62	20.06	5.00	−36395.29	0.97	−2.11	0.21	2.55	This work
Cs_3SbCl_6	11.89	2836.30	18.61	5.00	−65 248.10	1.0	−1.99	0.19	2.90	25
Rb_3SbBr_6	12.12	3008.35	17.18	5.00	−62136.79	0.96	−1.70	0.17	3.19	This work
Rb_3SbI_6	13.01	3717.55	12.78	5.00	−116285.70	0.94	−1.34	0.13	3.44	This work

geometry with Rb atoms occupying the Wyckoff positions (0.5, 0, 0), Sb atoms located at the center of the unit cell (0, 0, 0), and the halide anions (X = F, Cl, Br, I) positioned at (0.23, 0, 0).[25,37] Fig. 1(a–d) illustrate both the optimized crystal structures (inset) and the calculated energy–volume relationships for the cubic (C-phase) Rb_3SbX_6 compounds. To evaluate the structural properties of Rb_3SbX_6, input parameters including the lattice constant, space group symmetry, and precise atomic coordinates were required. Table 1 reports the optimized structural parameters and derived stability criteria for all compositions. In addition to the equilibrium bulk modulus B_0 (GPa), its pressure derivative $B_0^{'}$ represents a key mechanical property of the materials, indicating their resistance to volumetric compression under applied pressure. An increase in the lattice constants accompanied by a systematic decrease in B_0 (GPa) (as shown in Fig. 1(f)) is observed with substitution of the halide anion from F to I. This trend can be attributed to the increasing ionic radius of the halide species, which is consistent with previously reported results by M. Y. Khan *et al.*.[25] The bulk modulus B_0 (GPa) characterizes the material's incompressibility; a lower value indicates greater structural flexibility. Accordingly, the computed bulk moduli follow the sequence B_0 (Rb_3SbF_6) > B_0 (Rb_3SbCl_6) > B_0 (Rb_3SbBr_6) > B_0 (Rb_3SbI_6), reflecting the progressive softening of the lattice with larger halide ions. The nonlinear bulk modulus derivative $B_0^{'} = 5.00$ is commonly fixed during Birch–Murnaghan EOS fitting to ensure stable and consistent results, especially when limited energy–volume data is available. This standard approximation simplifies the fitting process without significantly affecting the accuracy for most solids. The density trend is governed by the competing effects of increasing molar mass (due to heavier halides and A-site cations like Cs) and expanding unit cell volume (due to larger ionic radii). Initially, volume dominates, lowering density (F → Cl), but later, mass gain offsets volume increase, leading to rising density (Cl → I).

Goldsmith's tolerance factor (τ_F) is employed to assess the structural stability of double perovskites. According to Goldsmith's criterion, a value approaching unity is indicative of an ideal, stable cubic structure (see Fig. 1(e)). In practice, the tolerance factor range of 0.8 to 1.0 is considered critical for the stabilization of cubic double perovskite phases. The calculated τ_F values for the investigated halide compounds fall within this stability window, as presented in Table 1, thereby confirming their potential stability in the cubic phase. To further validate their thermodynamic stability in the cubic configuration, the formation energies (ΔH_F) of Rb_3SbX_6 (X = F, Cl, Br, I) were computed.[31,38,39] The total energy of the Rb_3SbX_6 compounds is denoted as E (Rb_3SbX_6), while the reference energies of the constituent elements in their bulk phases are given by E (Rb), E (Sb), and E (X), where X = F, Cl, Br, or I. The resulting formation energies, (ΔH_F), are all negative, indicating that these compounds are thermodynamically stable and potentially amenable to experimental synthesis (see Fig. 1(e)).

3.2 Electronic properties

To explore the electronic characteristics of Rb_3SbX_6 (X = F, Cl, Br, I), band structure analyses were carried out using the modified Becke–Johnson (TB-mBJ) exchange–correlation potential. The choice of exchange correlation functional significantly impacts the accuracy of the computed bandgap, necessitating the use of TB-mBJ for more reliable predictions, as the PBE-GGA functional whose results may not align with the reported data. The band structures and corresponding total density of states (TDOS) were computed along key high-symmetry paths in the Brillouin zone and are depicted in Fig. 2.

The Fermi level was aligned at 0 eV for consistency. The valence band maximum (VBM) and conduction band minimum (CBM) are positioned at different high-symmetry locations, confirming the direct nature of the bandgaps. According to the TB-mBJ calculations, the bandgap energies were determined to be 5.47 eV for Rb_3SbF_6, 4.18 eV for Rb_3SbCl_6, 3.54 eV for Rb_3SbBr_6, and 2.85 eV for Rb_3SbI_6, all corresponding to direct transitions at the L–L points. These values categorize the materials as wide-bandgap semiconductors. Due to their wide bandgaps, halide double perovskites in this series are expected to exhibit low photon emission per absorbed photon, making them well-suited for ultraviolet (UV) optoelectronic applications. Such materials are particularly promising for use in UV photodetectors, UV light-emitting diodes, scintillation detectors, and related devices.[25,26]

To achieve a more detailed insight into the electronic band structure, it is essential to evaluate the specific contributions of the constituent atomic orbitals to the electronic bands. Accordingly, the partial density of states (PDOS) was computed and is displayed across an energy window from −6 eV to +6 eV, as shown in Fig. 3. The valence band spans approximately −6 eV to 0 eV, with its maximum situated at the Fermi level. The comparatively elevated density of states per electron volt in the valence band, as opposed to the conduction band, is indicative of the material's p-type character. The PDOS analysis indicates that the halide atoms (F, Cl, Br, I) make dominant contributions

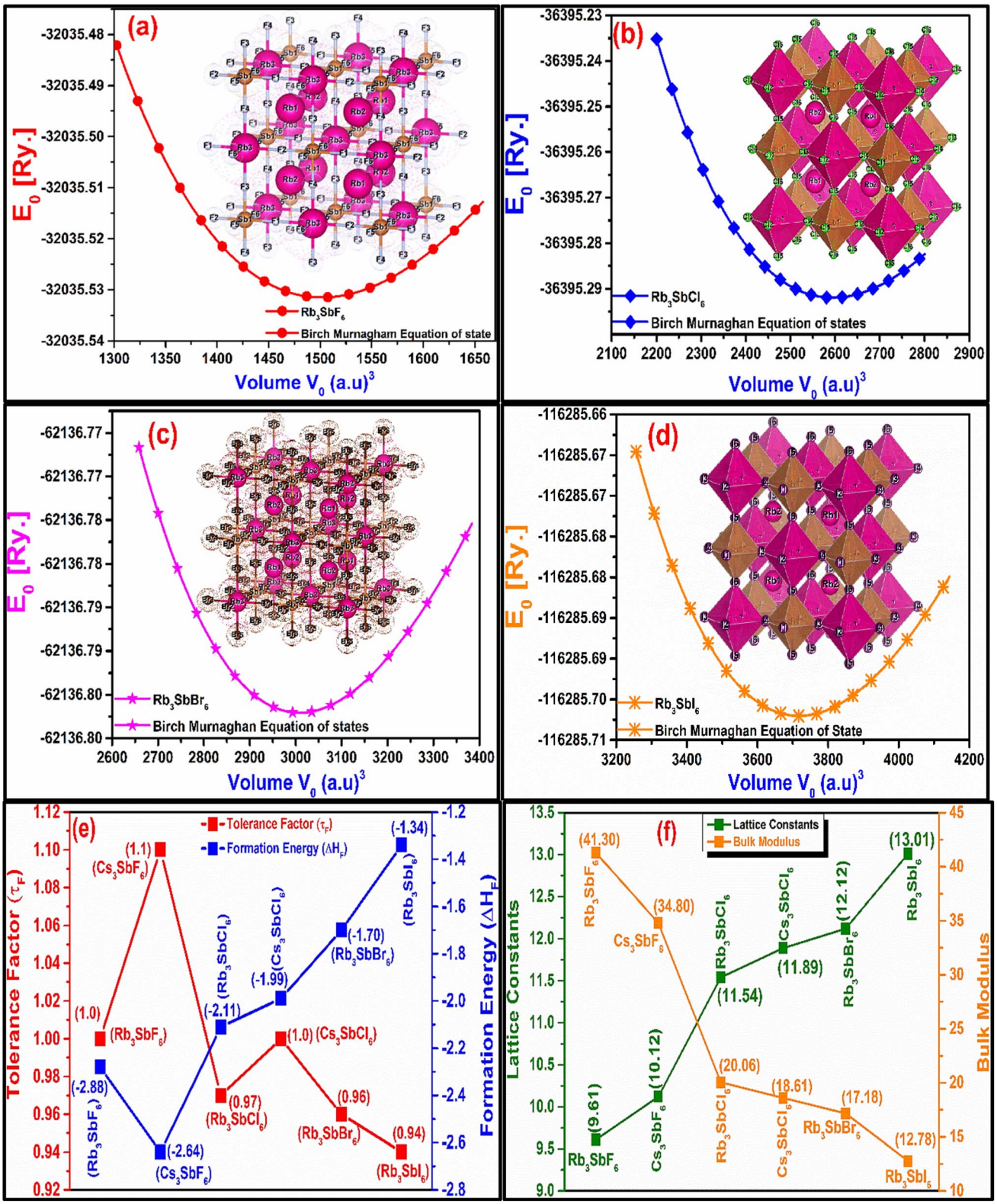

Fig. 1 (a–d) Crystal structure (inset graphs) and energy *vs.* volume plots (e) tolerance factor and formation energy (f) variation in lattice constants and bulk modulus for Rb_3SbX_6 (X = F, Cl, Br, I).

to the valence band through their p-orbitals, while the p-states of Rb and Sb exhibit minor contributions in the ranges of roughly (−6 to −3.89) eV, (−6 to −5.5) eV, and (−5.3 to 4) eV.

In contrast, the conduction band is largely derived from the p-orbitals of halides and Sb, with energy intervals observed at (−5.4 to 5.8) eV for Rb_3SbF_6, 4.2 to 4.5 eV for Rb_3SbCl_6, 3.6 to

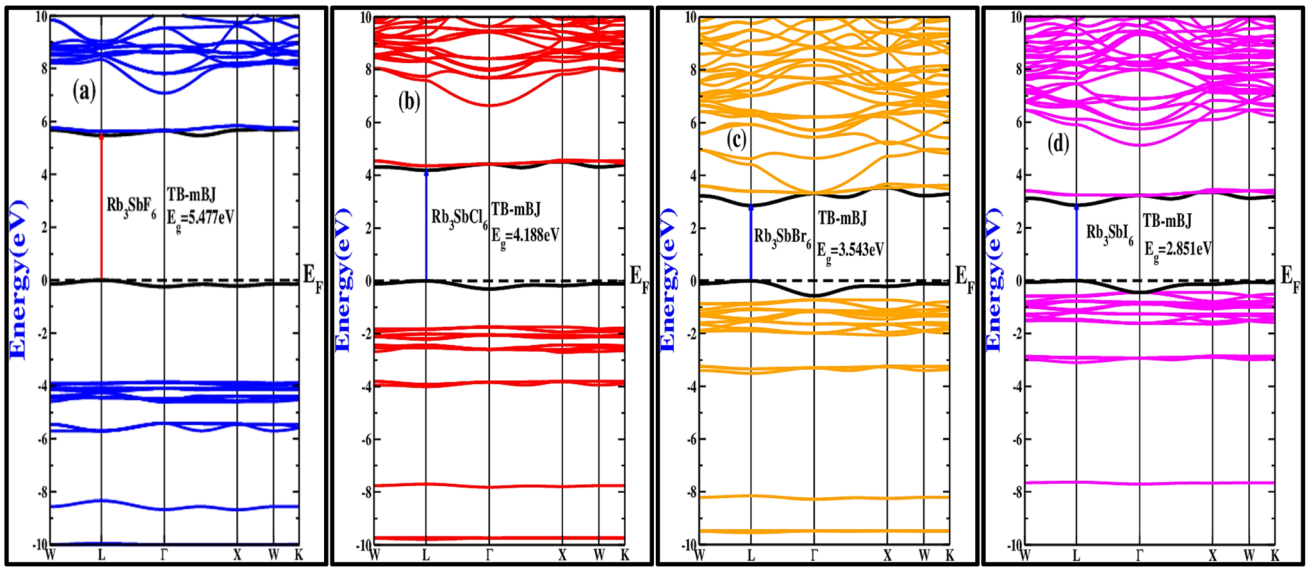

Fig. 2 Band structure plots of the Rb_3SbX_6 (a)–(d) (X = F, Cl, Br, I).

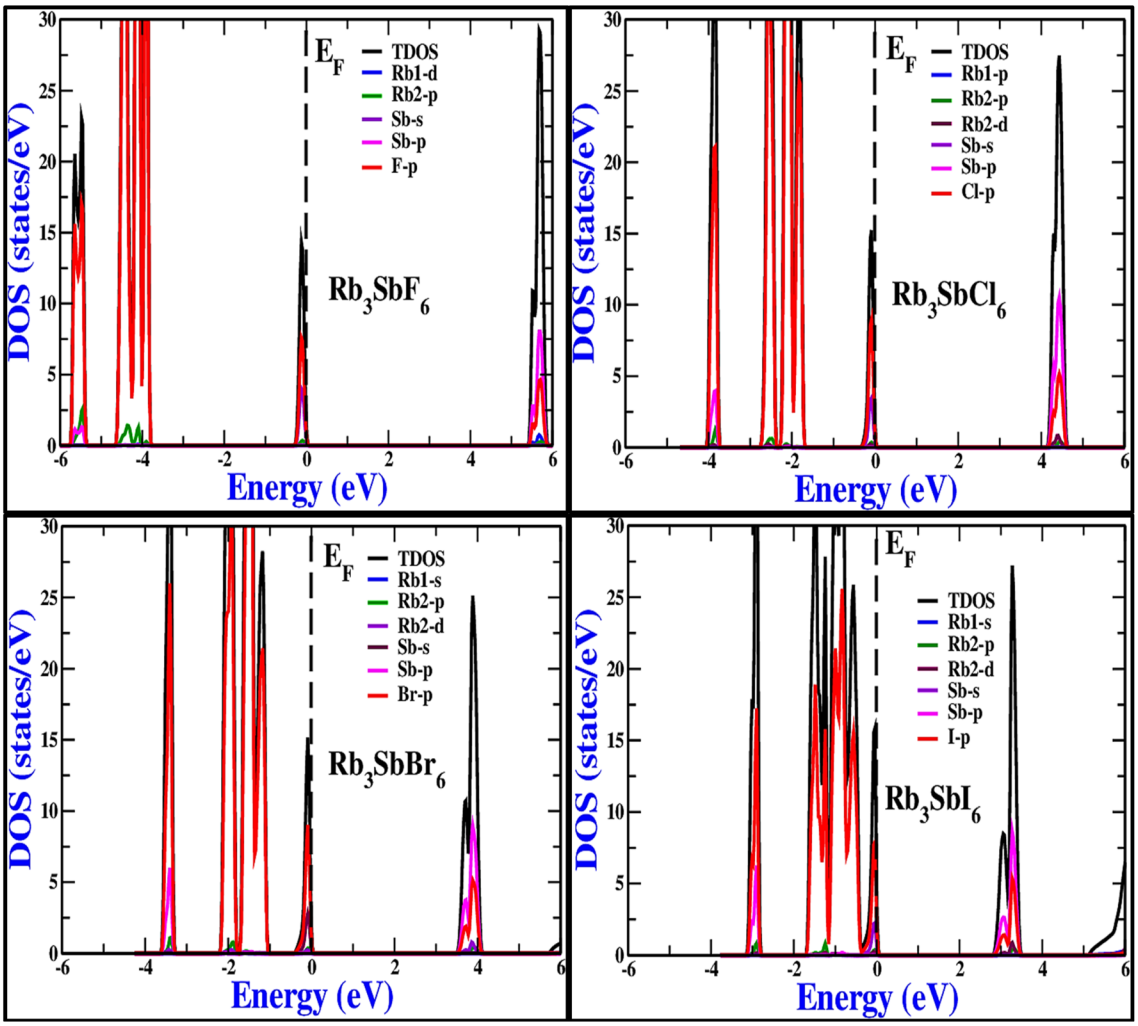

Fig. 3 DOS plots of Rb_3SbX_6 (X = F, Cl, Br, I).

4.1 eV for Rb_3SbBr_6, and 2.9 to 3.5 eV for Rb_3SbI_6. These results confirm the semiconducting properties of the Rb_3SbX_6 (X = F, Cl, Br, I) compounds, highlighting their potential utility in optoelectronic technologies. The computed density of states supports the presence of band gaps consistent with the semiconducting nature of these materials.[28]

Furthermore, the effective mass serves as an essential indicator for analyzing the electronic and optical characteristics of materials, such as their conductivity and carrier mobility. Since carrier mobility is inversely dependent on the effective masses of electrons and holes, larger effective mass values correspond to lower mobility.[40,41] Eqn (16) is employed to estimate the effective masses by performing a non-linear fit to the band structure (BS) data.

$$\frac{1}{m^*} = \frac{1}{\hbar^2}\frac{\partial^2 E}{\partial K^2} \tag{16}$$

In addition, the exciton binding energy (E_b^{ex}) was determined using the effective carrier masses along with the static (zero-frequency) dielectric constant $\varepsilon_1(0)$, as described by eqn (17). This energy quantifies the requirement to dissociate an exciton—a coulombically bound electron–hole pair into independent charge carriers. For photovoltaic applications, materials with lower exciton binding energies are advantageous, as they enable more efficient photon absorption and enhance charge separation and collection processes.

$$E_b^{ex} = \frac{e^4}{2\left(4pi\varepsilon_0\hbar^2\right)^2}\frac{\mu_r}{\varepsilon_1(0)^2} \approx 13.56\frac{\mu_r}{m_e}\frac{1}{\varepsilon_1(0)^2} \tag{17}$$

The effective masses and exciton binding energies for the Rb_3SbX_6 (X = F, Cl, Br, I) compounds are summarized in Table 2. Rb_3SbF_6 is found to exhibit higher electron and hole effective masses relative to Rb_3SbCl_6, Rb_3SbBr_6, and Rb_3SbI_6, indicating reduced carrier mobility and enhanced scattering or localization effects.[41] Moreover, the calculated exciton binding energies (E_b^{ex}) for Rb_3SbX_6 are substantially larger than those reported for Rb_2CuAsF_6 (0.29 eV)[42] and $In_2AgSbCl_6$ (0.058 eV).[43] These elevated binding energies suggest strong coulombic interactions between electrons and holes, highlighting the potential suitability of Rb_3SbX_6 compounds as absorber layers in photovoltaic applications.

3.3 Elastic properties

In perovskites, elastic properties describe the material's resistance to deformation and its mechanical stability under stress. Key parameters, such as elastic constants, bulk modulus, shear modulus, Young's modulus, Poisson's ratio, and Pugh's ratio are used to assess stiffness, compressibility, and ductility. These properties, often derived from DFT calculations, are essential for evaluating the structural reliability of perovskites in devices like solar cells, flexible electronics, and radiation detectors. The elastic properties of cubic halide double perovskites Rb_3SbX_6 (X = F, Cl, Br, I) were investigated through the calculation of their three independent elastic constants, which define the mechanical behavior of cubic crystals. These constants were employed to derive essential mechanical parameters, including the bulk modulus (B), shear modulus (G), Young's modulus (Y), Poisson's ratio (ν), elastic anisotropy factor (A), Cauchy's pressure (C_P), Lamé's constants (λ), the Voigt–Reuss–Hill averages (G_v, G_R), and the Grüneisen parameter (γ). The Born stability criteria were applied to assess the mechanical stability of the compounds, imposing specific constraints on the elastic constants (C_{ij}).[29]

$$C_{11} > 0,\ C_{44} > 0,\ (C_{11} + 2C_{12}) > 0 \text{ and } C_{11} - C_{12} > 0 \tag{18}$$

The calculated bulk modulus and elastic constants of the studied compounds meet the mechanical stability criteria, confirming their mechanical robustness. The elastic properties, including the bulk modulus (B), shear modulus (G), Young's modulus (Y), and Poisson's ratio (υ), were subsequently derived using standard theoretical formulations.

$$B = \frac{C_{11} + 2C_{12}}{3} \tag{19}$$

$$G = \frac{G_V + G_R}{2} \tag{20}$$

$$Y = \frac{9BG_V}{3B + G_V} \tag{21}$$

$$\upsilon = \frac{3B - 2G}{2(3B + 2G)} \tag{22}$$

Reuss-modulus (G_R), Viogt modulus (G_V), could also be easily computed using the expressions

$$G_R = \frac{5C_{44}(C_{11} - C_{12})}{4C_{44} + 3(C_{11} - C_{12})} \tag{23}$$

$$G_V = \frac{1}{5}(C_{11} - C_{12} + 4C_{44}) \tag{24}$$

The bulk modulus B (GPa), which quantifies a material's resistance to volumetric compression under applied pressure,[44] exhibits a systematic decrease down the halide series. As presented in Table 3, Rb_3SbI_6 shows the lowest B (GPa) value, indicating higher compressibility compared to $Rb_3Sb(F/Cl/Br)_6$ (X = F, Cl, Br). Notably, Rb_3SbF_6 displays the highest bulk modulus (40.82 GPa), suggesting enhanced resistance to volume reduction and greater intrinsic hardness relative to the iodide analogue. The shear modulus G(GPa), reflecting resistance to shape deformation under shear stress, was also

Table 2 Effective masses and exciton binding energies of Rb_3SbX_6 (X = F, Cl, Br, I)

Parameters	Method	Rb_3SbF_6	Rb_3SbCl_6	Rb_3SbBr_6	Rb_3SbI_6
m_h^*	TB-mBJ	0.157	0.120	0.059	0.061
m_e^*	TB-mBJ	0.159	0.092	0.039	0.045
E_b^{ex}	TB-mBJ	2.877	1.676	1.234	0.703

Table 3 Computed elastic properties of Rb_3SbX_6 (X = F, Cl, Br, I)[a]

	This work				Other work	
Compounds	Rb_3SbF_6	Rb_3SbCl_6	Rb_3SbBr_6	Rb_3SbI_6	Cs_3SbF_6	Cs_3SbCl_6
C_{11}	85.25	46.29	41.63	30.34	43.40 (ref. 25)	24.22 (ref. 25)
C_{12}	18.60	5.40	5.00	3.26	8.77 (ref. 25)	3.79 (ref. 25)
C_{44}	3.09	3.46	11.60	3.73	3.43 (ref. 25)	1.46 (ref. 25)
Bulk modulus B_H [GPa]	40.82	19.03	17.21	12.28	20.31 (ref. 25)	10.60 (ref. 25)
Shear modulus G_H [GPa]	10.01	7.72	13.94	6.45	7.02 (ref. 25)	6.60 (ref. 25)
Young's modulus Y_H [GPa]	27.77	20.41	32.93	16.48	18.88 (ref. 25)	9.69 (ref. 25)
Poisson ratio ν_H	0.39	0.32	0.18	0.28	0.35 (ref. 25)	0.35 (ref. 25)
Pugh's ratio B/G	4.08	2.46	1.23	1.90	2.89 (ref. 25)	2.95 (ref. 25)
Cauchy pressure $C_p = C_{12} - C_{44}$	15.52	1.93	−6.60	−0.48	5.34 (ref. 25)	2.33 (ref. 25)
Kleinman parameter ξ	0.37	0.27	0.27	0.26	0.35 (ref. 25)	0.31 (ref. 25)
Anisotropy A	0.09	0.17	0.63	0.28	0.20 (ref. 25)	0.14 (ref. 25)
Melting temperature T_m [K]	1056.82	826.56	799.05	732.28	809.49 (ref. 25)	696.11 (ref. 25)
Debye temperature θ_D [K]	187.40	177.37	235.21	120.01	60.99 (ref. 25)	52.95 (ref. 25)
Transverse velocity v_t [m s^{-1}]	1736.49	1839.05	2250.40	1413.03	557.50 (ref. 25)	552.14 (ref. 25)
Longitudinal velocity v_L [m s^{-1}]	3841.78	3391.07	3349.85	2367.41	2703.31 (ref. 25)	2304.42 (ref. 25)
Mean velocity v_m [m s^{-1}]	1958.10	2052.02	2457.67	1563.95	637.25 (ref. 25)	630.60 (ref. 25)
Lamé 1st constant λ	34.14	13.88	7.92	7.98	15.63 (ref. 25)	8.20 (ref. 25)
Lamé 2nd constant μ	15.66	12.42	24.17	10.61	11.17 (ref. 25)	5.72 (ref. 25)
Grüensien parameter γ	1.75	2.05	2.58	2.24	1.95 (ref. 25)	1.93 (ref. 25)
Machinability μ_M	13.22	5.49	1.48	3.29	—	—
Thermal expansion α	1.60×10^{-4}	2.07×10^{-4}	1.15×10^{-4}	2.48×10^{-4}	—	—

[a] Ref. 25.

evaluated (Table 3). Rb_3SbBr_6 exhibits the highest shear modulus (13.94 GPa), substantially exceeding that of Rb_3SbI_6 (6.45 GPa), indicating superior rigidity against shear-induced distortions. Young's modulus Y (GPa) provides an additional measure of elastic stiffness. Higher Y-values correspond to greater stiffness, hardness, and resistance to elastic deformation.[45] According to Table 3, Rb_3SbBr_6 attains the highest Young's modulus (32.93 GPa), while Rb_3SbI_6 has the lowest (16.48 GPa), underscoring the enhanced mechanical robustness of the bromide phase. Furthermore, the shear modulus G is critical in assessing dynamic stability, as it indicates resistance to tetragonal distortions. The computed GGG values for all Rb_3SbX_6 (X = F, Cl, Br, I) compounds are summarized in Table 3. An important elastic parameter for evaluating the angular nature of atomic bonding is the Cauchy pressure C_P.[46] A negative C_P is generally associated with ionic bonding, whereas a positive value suggests covalent character. Materials with more pronounced directional bonding typically exhibit lower atomic mobility as C_P becomes increasingly negative. C_P was calculated using the relation ($C_P = C_{12} - C_{44}$) (see Table 3). Positive C_P values obtained for Rb_3SbF_6 and Rb_3SbCl_6 indicate covalent bonding tendencies and imply ductile behavior ($C_P > 0$). In contrast, negative C_P values observed for Rb_3SbBr_6 and Rb_3SbI_6 reflect ionic bonding characteristics and suggest a brittle nature ($C_P < 0$). Further insight into ductility and brittleness is provided by the Poisson's ratio (ν)[47] and Pugh's ratio (B/G).[48] Typically, materials with $\nu > 0.26$ and $B/G > 1.75$ exhibit ductile behavior. For the Rb_3SbX_6 (X = F, Cl, Br, I) series, most compounds show Poisson's ratios exceeding 0.26 and Pugh's ratios above the critical threshold, confirming their ductile nature. However, Rb_3SbBr_6 exhibits a Poisson's ratio of 0.18 and a Pugh's ratio of 1.28, indicating a tendency toward brittleness (see Table 3). The Zener anisotropy factor (A) provides a quantitative assessment of elastic anisotropy in crystalline solids, with $A = 1$ characterizing an ideal isotropic medium.[36] Deviations from unity indicate the presence and degree of elastic anisotropy. As shown in Table 3, the calculated values of A for the studied materials differ from one, confirming their anisotropic elastic behavior.

$$\text{Zener Anisotropic Factor} = A = \frac{2C_{44}}{(C_{11} - C_{12})} \tag{25}$$

Elastic anisotropy is a fundamental factor influencing the prediction of micro-hardness and mechanical robustness in crystalline materials. Elevated levels of elastic anisotropy are often associated with an increased propensity for microcrack formation, thereby compromising structural integrity. It is noteworthy that even materials crystallizing in cubic symmetry can exhibit significant deviations from isotropic elastic behavior. Fine *et al.*[49] established a notable relationship between the melting temperature (T_m) and the elastic constant C_{11} for cubic crystalline materials.

$$T_m = [500 + (5.91\ \text{K GPa}^{-1})C_{11}] \mp 300\ \text{K} \tag{26}$$

Table 3 shows that Rb_3SbI_6 possesses the lowest melting temperature (T_m) among the studied compounds, measured at 732.28 K. Although this represents the minimum value within the series, it still indicates considerable thermal stability. In comparison, the other compounds exhibit markedly higher melting temperatures. The Kleinman parameter, ζ, which

characterizes the internal strain of the crystal lattice,[50] is determined using the following expression:

$$\zeta = \frac{C_{11} + 8C_{12}}{7C_{11} + 2C_{12}} \quad (27)$$

Table 3 summarizes the comparative ease of bond bending relative to bond stretching in the Rb_3SbX_6 (X = F, Cl, Br, I) double perovskites. The Kleinman parameter (ζ) quantifies this behavior, with $\zeta = 0$ representing pure bond bending and $\zeta = 1$ indicating pure bond stretching. The calculated ζ values for these compounds lie in the range 0–0.4, demonstrating that bond bending is energetically more favorable than bond stretching. Values approaching unity would imply a dominant bond-stretching character, which is not observed here.

For isotropic materials, the Lamé coefficients are defined as $\lambda = C_{12}$ and $\mu = G$.[51] However, the Rb_3SbX_6 compounds exhibit anisotropy, as evidenced by their calculated elastic constants in Table 3, and thus do not satisfy the conditions for isotropy. Table 3 also reports the computed sound velocities and Debye temperatures Θ_D (K) for these materials. The average sound velocity (V_m) was determined by combining the transverse (v_t) and longitudinal (v_L) components, applying the Navier equation of state (NEOS).[52,53] The Debye temperature was then estimated using the mean acoustic velocity according to established methods. The relative Debye temperatures provide insight into lattice dynamical stability across different temperatures. For example, Rb_3SbI_6 exhibits a Debye temperature of 120.01 K, suggesting enhanced stability at low temperatures, consistent with prior correlations between Θ_D (K) and vibrational properties.[54]

$$\theta_D = \frac{h}{k_B}\left\{\frac{3nN_A\rho}{4\pi M}\right\}^{1/3} v_m \quad (28)$$

In eqn (28), N_A denotes Avogadro's number, k_B is the Boltzmann constant, ρ is the density of the material, M is the molecular mass, and v_m represents the mean sound velocity. The calculated Debye temperatures for Rb_3SbX_6 (X = F, Cl, Br, I) are listed in Table 3. Among these, Rb_3SbBr_6 exhibits a higher Debye temperature than Rb_3SbF_6, Rb_3SbCl_6, and Rb_3SbI_6. As the Debye temperature is directly related to the lattice specific heat capacity, this result suggests that Rb_3SbBr_6 has an improved ability to accommodate thermal energy arising from lattice vibrations.[53,54] The thermodynamic stability of these compounds is also temperature-dependent. The Grüneisen parameter,[30] given by $\left[\gamma = \frac{3(1+\nu)}{2(2-3\nu)}\right]$, was determined for Rb_3SbX_6 using the Poisson's ratio (ν). This parameter provides insight into the anharmonicity of lattice vibrations and influences key physical properties such as thermal conductivity, thermal expansion, high-temperature elastic behavior, and acoustic wave attenuation. The estimated values of the Grüneisen parameter for the Rb_3SbX_6 series are also presented in Table 3.

The thermal expansion coefficient (α) is closely linked to properties such as thermal conductivity (k), specific heat, band gap temperature dependence, and electron effective mass (m_e^*). Precise knowledge of α is essential for controlling strain during epitaxial growth and minimizing defects in electronic and spintronic devices. The coefficient can be evaluated using the following relation.[55]

$$\alpha = \frac{1.6 \times 10^3}{G} \quad (29)$$

The empirical relation $\alpha \approx 0.02/T_m$[56] describes the inverse correlation between melting temperature and thermal expansion. For Rb_3SbX_6 (X = F, Cl, Br, I), calculated α values ($\times 10^{-4}$ K^{-1}) are 1.60 (F), 2.07 (Cl), 1.15 (Br), and 2.48 (I). Table 3 shows Rb_3SbBr_6 has lower α than Rb_3SbCl_6, consistent with its higher T_m.

Machinability describes the ease with which a solid can be shaped or cut using standard tooling, and is commonly quantified by the machinability index ($\mu_M = B/C_{44}$), which also serves as an indicator of plasticity and dry lubrication performance. Higher μ_M values correspond to improved dry lubricating behavior and reduced friction. The calculated μ_M values for Rb_3SbX_6 (X = F, Cl, Br, I) compounds (Table 3) indicate generally good machinability, with Rb_3SbF_6 exhibiting the highest index. This favorable behavior is attributed to their mixed ionic–covalent bonding, suggesting suitability for applications requiring effective shaping and low-friction properties.[57]

To assess the elastic anisotropy of Rb_3SbX_6 (X = F, Cl, Br, I) double perovskites, three-dimensional (3D) and two-dimensional (2D) contour plots were generated using the ELATE Tensor Analysis code[58] based on the calculated elastic stiffness coefficients (C_{ij}). In isotropic crystals, such representations appear as perfect spheres, indicating uniform mechanical response. However, the pronounced deviations from spherical symmetry observed in Rb_3SbX_6 highlight significant directional dependence in their elastic properties.[59] Fig. 4 displays the 2D and 3D visualizations of the Young's modulus (Y), shear modulus (G, in GPa), and Poisson's ratio (ν), clearly revealing the degree of anisotropy inherent in these compounds.[25] The present work reports the computed and graphically illustrated minimum and maximum values of Young's modulus (Y), shear modulus (G) (in GPa), and Poisson's ratio (ν) for Rb_3SbX_6 (X = F, Cl, Br, I) in different crystallographic orientations, as summarized in Table 4.

The anisotropy of these elastic parameters follows the order Rb_3SbF_6 > Rb_3SbCl_6 > Rb_3SbI_6 > Rb_3SbBr_6. Notably, Rb_3SbCl_6 (26.94) demonstrates the highest Poisson anisotropy among the series, followed by Rb_3SbI_6 (15.86), Rb_3SbBr_6 (3.98), and Rb_3SbF_6 (3.20). The anisotropy of Rb_3SbF_6 (8.96) Young's modulus is lower than that of Rb_3SbCl_6 (4.61), Rb_3SbBr_6 (1.42), and Rb_3SbI_6 (2.92). Generally, Rb_3SbBr_6 exhibits the least anisotropy, as the three-dimensional representations of all moduli approximate a spherical shape, while Rb_3SbCl_6 displays the highest anisotropy, with its 3D graphs of all moduli significantly deviating from a spherical form. Such numerical and graphical analyses are essential for elucidating the orientation-dependent elastic behavior of Rb_3SbX_6 compounds. These results have significant implications for the design and optimization of materials with tailored mechanical performance, ensuring structural stability and reliability under diverse loading conditions.[25,43]

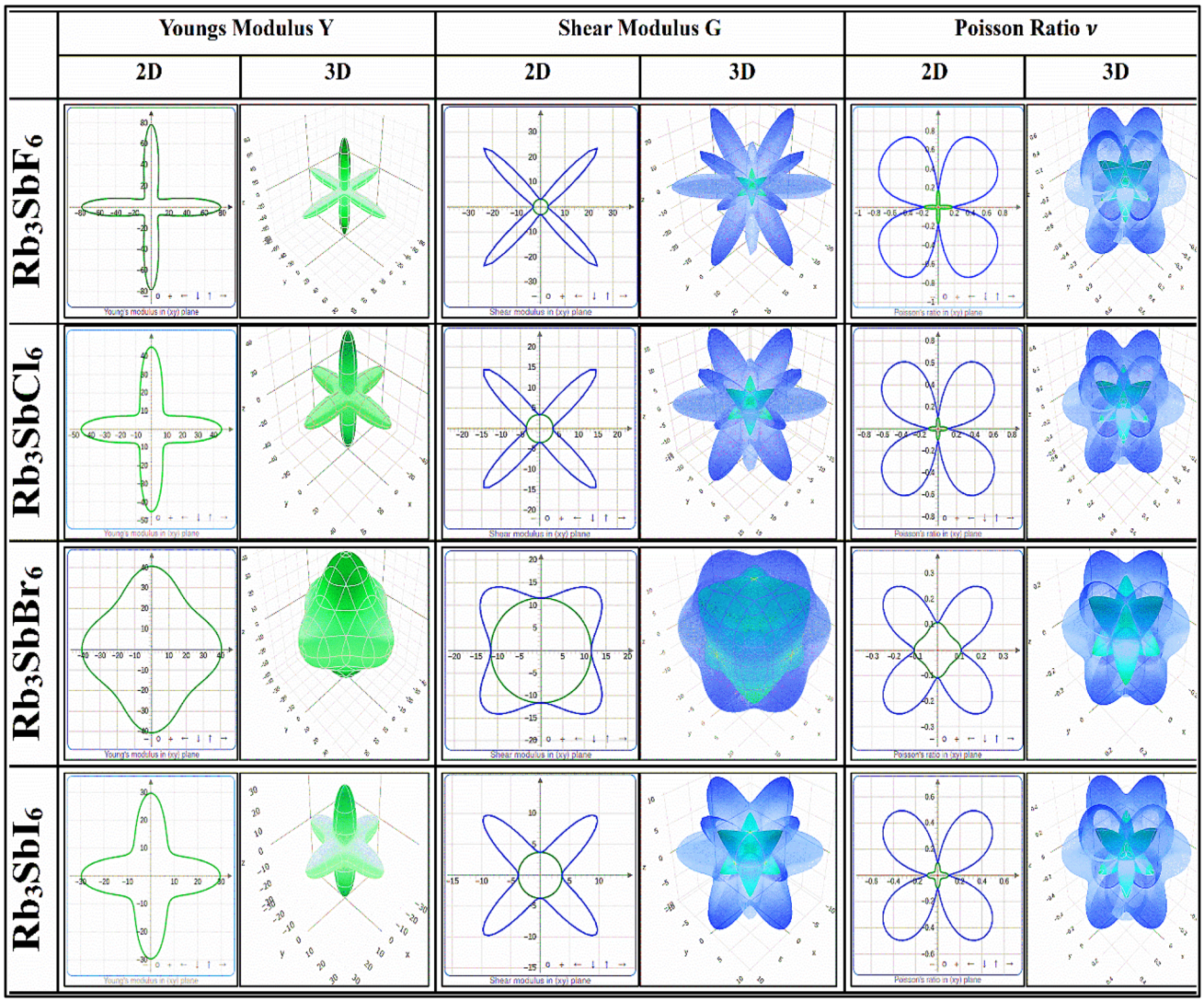

Fig. 4 2D & 3D plots of the elastic moduli of the Rb_3SbX_6 (X = F, Cl, Br, I).

Table 4 Maximum and minimum values for shear modulus in GPa, Young's modulus in GPa, and Poison ratio along with anisotropy in GPa for Rb_3SbX_6 (X = F, Cl, Br, I)[a]

	This work				Other work	
Parameters	Rb_3SbF_6	Rb_3SbCl_6	Rb_3SbBr_6	Rb_3SbI_6	Cs_3SbF_6	Cs_3SbCl_6
G_{min}	3.09	3.46	11.60	3.73	3.43 (ref. 25)	1.46 (ref. 25)
G_{max}	33.32	20.44	18.31	13.54	17.31 (ref. 25)	10.21 (ref. 25)
A	10.78	5.90	1.57	3.63	5.04 (ref. 25)	6.69 (ref. 25)
Y_{min}	9.04	9.78	28.41	10.16	9.74 (ref. 25)	4.18 (ref. 25)
Y_{max}	78.58	45.16	40.55	29.70	40.45 (ref. 25)	23.19 (ref. 25)
A	8.96	4.61	1.42	2.92	4.15 (ref. 25)	5.53 (ref. 25)
ν_{min}	0.02	0.02	0.08	0.03	0.04 (ref. 25)	0.03 (ref. 25)
ν_{max}	0.87	0.75	0.32	0.63	0.75 (ref. 25)	0.80 (ref. 25)
A	3.20	26.94	3.98	15.86	15.06 (ref. 25)	26.15 (ref. 25)

[a] Ref. 25.

3.4 Optical characteristics

The real and imaginary components of the dielectric function were computed to elucidate the radiation response of the halide double perovskites Rb_3SbX_6 (X = F, Cl, Br, I), as presented in Fig. 5(a). The calculated dielectric spectra cover the photon energy range from 0 to 12 eV. The static dielectric constant, $\varepsilon(0)$,

was determined to be 1.53 for Rb_3SbF_6, 2.15 for Rb_3SbCl_6, 2.62 for Rb_3SbBr_6, and 3.40 for Rb_3SbI_6. Beyond the static limit, all compositions exhibit rising dielectric values, reaching prominent peaks of 4.53 at 5.53 eV (Rb_3SbF_6), 5.01 at 4.28 eV (Rb_3SbCl_6), 5.31 at 3.65 eV (Rb_3SbBr_6), and 6.35 at 2.97 eV (Rb_3SbI_6). Additional minor features are observed in the 4.20–9.42 eV region, with calculated values of 2.62 (9.42 eV), 2.99 (6.08 eV), 5.01 (5.51 eV), and 5.14 (4.20 eV), respectively, as shown in Fig. 5(a). Following these maxima, the dielectric response displays further increases, with several local peaks attributable to interband electronic transitions. Negative values of the real part of the dielectric function were calculated in the 4.56–7.56 eV and 9.39–12 eV ranges, indicating metallic-like behavior in these energy intervals in line with the predictions of Penn's model. The occurrence of negative values in the real part of the dielectric function, $\varepsilon_1(\omega)$, is attributed to intense interband electronic transitions that significantly influence the optical characteristics of the material. These negative values suggest that, at certain photon energies, the material exhibits behaviour similar to that of metals, where electromagnetic waves are predominantly reflected rather than transmitted. This phenomenon results from the Kramers–Kronig relations, which connect the real and imaginary components of the dielectric function. When the imaginary part, $\varepsilon_2(\omega)$, displays pronounced absorption peaks due to electronic excitations, it can lead to corresponding negative dips in $\varepsilon_1(\omega)$. Such features are common in materials with strong electronic interactions and reflect their complex light–matter interactions. A negative real part of the dielectric function in a narrow UV range is typically caused by strong interband transitions rather than true metallicity, and reflects dispersive optical behavior rather than free-electron conduction. Fig. 5(b) shows the threshold and peak energies of the imaginary part of the dielectric function, $\varepsilon_2(\omega)$, for the Rb_3SbX_6 series. The threshold energies of $\varepsilon_2(\omega)$ were found to be 5.26 eV (Rb_3SbF_6), 4.01 eV (Rb_3SbCl_6), 3.36 eV (Rb_3SbBr_6), and 2.67 eV (Rb_3SbI_6). The corresponding maximum $\varepsilon_2(\omega)$ values reached 5.41 at 5.78 eV, 5.98 at 6.92 eV, 6.61 at 5.78 eV, and 7.50 at 4.50 eV. These peaks become increasingly pronounced at higher energies, approaching the ultraviolet region, which suggests potential for optoelectronic applications within that spectral range.[25]

In Fig. 5(c), the computed energy-dependent refractive index $n(\omega)$ is presented, which is influenced by the real part of the dielectric function, incident photon energy, and intrinsic material composition. The refractive index provides essential insight into the optical response of the material by quantifying the degree of light bending as it propagates through the medium.[60,61] The static refractive index values $n(0)$ for Rb_3SbX_6 (X = F, Cl, Br, I) are found to be 1.24, 1.46, 1.62, and 1.84, respectively. A progressive increase in $n(\omega)$ is observed with increasing energy, reaching peak values of 2.22 at 5.56 eV (Rb_3SbF_6), 2.33 at 6.74 eV (Rb_3SbCl_6), 2.35 at 3.65 eV (Rb_3SbBr_6), and 2.56 at 3.02 eV (Rb_3SbI_6). Beyond these maxima, $n(\omega)$ exhibits multiple local fluctuations, with notable peaks occurring at 1.66 (9.47 eV), 2.30 (4.32 eV), 1.94 (8.87 eV), and 2.39 (4.24 eV) for the respective halide compositions. Fig. 5(d) illustrates the extinction coefficient $K(\omega)$, which corresponds to the imaginary component of the complex refractive index and signifies that how much light is absorbed when light travels through the material. The threshold onset of $K(\omega)$ occurs at 5.17 eV, 3.94 eV, 3.36 eV, and 2.64 eV for Rb_3SbF_6, Rb_3SbCl_6, Rb_3SbBr_6, and Rb_3SbI_6, respectively, with corresponding peak values of 1.68 (5.87 eV), 1.76 (7.04 eV), 1.81 (5.88 eV), and 1.90 (4.58 eV). Secondary features are observed at 1.27 (10.25 eV), 1.39 (4.59 eV), 1.27 (4.06 eV), and 1.23 (3.41 eV), further confirming the optical activity in the near-UV region. These observations are consistent with the behavior of the imaginary part of the dielectric function $\varepsilon_2(\omega)$ and the absorption coefficient $\alpha(\omega)$, which demonstrate significant optical transitions near the ultraviolet threshold. Reflectivity, which quantifies a material's capability to reflect incident electromagnetic radiation, is a crucial parameter for optoelectronic applications and energy-efficient design. In general, metals exhibit higher reflectivity due to the abundance of free carriers, whereas semiconductors demonstrate lower values. The low reflectivity observed across the studied Rb_3SbX_6 (X = F, Cl, Br, I) compounds confirms their semiconducting character.[25,31]

Optical conductivity $\sigma(\omega)$ characterizes charge-carrier dynamics under optical excitation. Fig. 5(e) presents the simulated $\sigma(\omega)$ spectra for lead-free halide double perovskites Rb_3SbX_6 (X = F, Cl, Br, I). In all cases, $\sigma(\omega)$ remains negligible below the optical band gap, with calculated cutoff energies of 5.09 eV (Rb_3SbF_6), 3.93 eV (Rb_3SbCl_6), 3.26 eV (Rb_3SbBr_6), and 2.65 eV (Rb_3SbI_6). Maximum optical conductivities are observed at 4215.77 Ω^{-1} cm^{-1} (5.77 eV), 5573.59 Ω^{-1} cm^{-1} (6.90 eV), 5164.38 Ω^{-1} cm^{-1} (5.78 eV), and 4894.68 Ω^{-1} cm^{-1} (7.50 eV), respectively. The absorption coefficient $\alpha(\omega)$, shown in Fig. 5(f), describes the material's capacity to attenuate incident radiation.[62,63] The absorption edges are determined as 5.21 eV (Rb_3SbF_6), 4.00 eV (Rb_3SbCl_6), 3.38 eV (Rb_3SbBr_6), and 2.70 eV (Rb_3SbI_6). All compounds exhibit pronounced absorption in the ultraviolet region, with primary peaks at 132.15 $\times$ 10^4 cm^{-1} (10.25 eV), 126.57 $\times$ 10^4 cm^{-1} (7.05 eV), 108.90 $\times$ 10^4 cm^{-1} (5.88 eV), and 120.37 $\times$ 10^4 cm^{-1} (9.63 eV), confirming strong UV absorption behavior relevant for optoelectronic applications.[25]

Fig. 5(g) displays the calculated energy loss function, L(ω), for the Rb_3SbX_6 (X = F, Cl, Br, I) double perovskites. The results reveal that energy loss is maximum in regions where the absorption coefficient attains its maximum, indicating that $L(\omega)$ exerts limited influence on the overall optical response of these materials. The computed $L(\omega)$ peak values are 5.09 at 10.73 eV for Rb_3SbF_6, 3.06 at 7.58 eV for Rb_3SbCl_6, 2.39 at 6.42 eV for Rb_3SbBr_6, and 1.70 at 5.13 eV for Rb_3SbI_6. These comparatively high peak intensities suggest that the energy loss function substantially affect the absorption behavior of the examined compounds. The optical analysis thus indicates that these lead-free halide double perovskites are promising candidates for light-harvesting optoelectronic applications, given their strong absorption, favorable dispersion, low reflectivity in the visible range, and minimal energy loss in the near-ultraviolet region.[64]

Reflectivity, defined as the ratio of incident to reflected radiation intensity,[61,65] is illustrated in Fig. 5(h). The $R(\omega)$ spectra show lower reflectivity values in the visible range relative to the near-UV region, and are 1%, 3%, 6%, and 9% for the

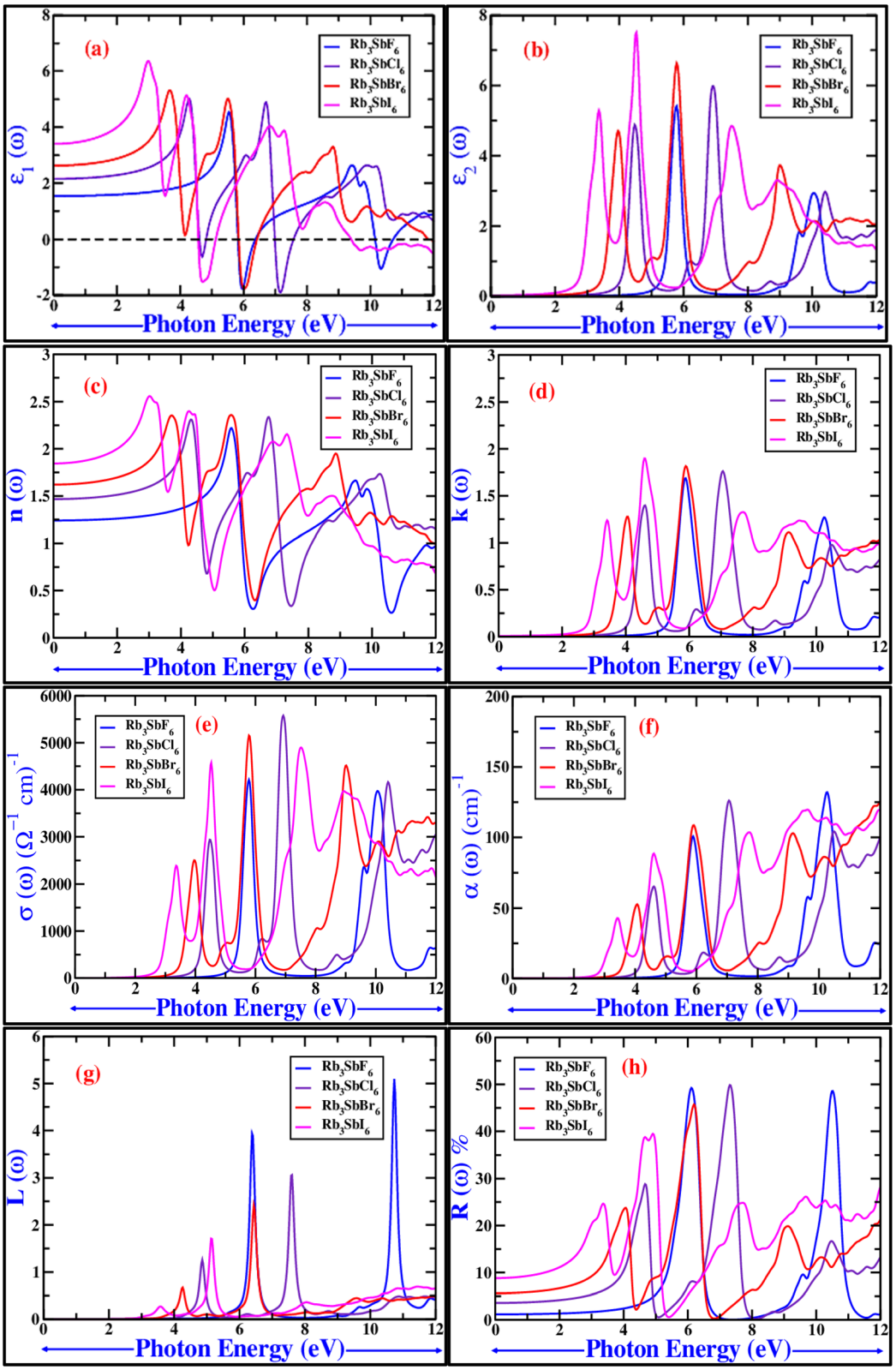

Fig. 5 (a–h) Optical plots of the Rb_3SbX_6 (X = F, Cl, Br, I) compounds.

Rb_3SbX_6 (X = F, Cl, Br, I) at normal incidence. As evident from Fig. 5(h), all investigated Rb_3SbX_6 compounds exhibit strong absorption in the ultraviolet region. The maximum reflectivity peaks are calculated to be 49.10 at 6.12 eV for Rb_3SbF_6, 49.86 at 7.30 eV for Rb_3SbCl_6, 45.77 at 6.17 eV for Rb_3SbBr_6, and 39.44 at 4.91 eV for Rb_3SbI_6. These findings highlight the potential of

these materials for application in ultraviolet photodetectors, light-emitting diodes, photovoltaic devices, and other optoelectronic technologies. Moreover, increased ultraviolet irradiation enhances absorption, while energy loss remains a critical consideration, as it represents a pathway for energy dissipation that can reduce device efficiency.[25]

3.5 Light yield

The light yield (LY), which defines the scintillation response of the materials examined in this study, constitutes a fundamental parameter for evaluating the performance of scintillators and phosphors. The computed number of photons emitted per MeV of absorbed radiation energy provides a quantitative basis for comparing scintillation efficiency. A higher LY, in conjunction with an improved signal-to-noise ratio, is particularly desirable for the reliable detection of low-energy or low-intensity radiation. This equation estimates the light yield of the scintillating material based on a phenomenological model describing the mechanisms governing detected light emission in scintillators.

$$\mathrm{LY} = \frac{SQ}{\beta E_g} \times 10^6 \text{photons per MeV} \quad (30)$$

The energy transfer efficiency is denoted by S, and the quantum efficiency by Q, while β and the band gap (E_g, in eV) are considered constant. The energy required to generate an electron–hole (e–h) pair is expressed as βE_g. Typically, β ranges between 1.5 and 2 for most materials, whereas for covalent materials it generally lies between 3 and 4. Empirical relationships derived from experimental studies of various scintillators justify fixing β at 2.5. Using $\beta = 2.5$ under ideal conditions (*i.e.*, $S = Q = 1$), the light yield (LY) of the studied compounds can be straightforwardly estimated. The values presented in Table 5 thus represent the theoretical maximum LY achievable by these materials. It should be noted that, under ideal circumstances, the actual LY may slightly exceed these calculated values due to internal reflection effects within the crystal. Among the compounds investigated, Rb_3SbI_6 exhibits particularly high LY values in the ultraviolet and higher-energy regions, highlighting its potential as a promising candidate for high-power radiation detection, scintillation and other optoelectronic applications.[25,26]

3.6 Thermodynamic properties

A practical method for assessing the thermodynamic properties of materials employs the GIBBS program.[66] In this work, the macroscopic thermal behavior of Rb_3SbX_6 (X = F, Cl, Br, I) was evaluated as a function of pressure (P, GPa) and temperature (T, K).[35] Fig. 6 (top left) shows the calculated unit cell volume as a function of temperature (200–600 K) at two pressures: 0 GPa (blue curves) and 10 GPa (red curves), obtained using the quasi-harmonic approximation. At 0 GPa, all compositions exhibit an approximately linear increase in volume with temperature, consistent with expected thermal expansion arising from lattice vibrations. The absolute volume at ambient pressure increases systematically from Rb_3SbF_6 to Rb_3SbI_6, reflecting the larger ionic radii of heavier halides. Under 10 GPa, the unit cell volumes decrease due to compression, with a reduced temperature dependence that indicates suppression of thermal expansion and diminished lattice anharmonicity at elevated pressure. The volume difference between 0 GPa and 10 GPa is more pronounced for Cl, Br, and I, suggesting greater compressibility associated with the heavier halide ions.[35] The temperature range of 200–600 K is selected because it aligns with the typical operational and stability conditions of halide perovskites in practical applications such as solar cells, photodetectors, and scintillation devices. Within this range, the materials remain in their thermodynamically stable phase, avoiding decomposition or phase transitions that often occur at higher temperatures. Moreover, this range is ideal for applying the quasi-harmonic approximation, which provides reliable predictions of thermodynamic properties like entropy and Gibbs free energy at low to moderate temperatures. It also facilitates direct comparison with experimental data, as most thermal characterization techniques operate effectively within this temperature range. At ambient pressure (~0.1 MPa), the trends in both volume and bulk modulus and other parameter closely follow those at 0 GPa, showing negligible deviation. Therefore, the 0 GPa data effectively represent ambient pressure behaviour.

Fig. 6 (top right) depicts the temperature dependence of the bulk modulus for Rb_3SbX_6 under 0 GPa and 10 GPa, also calculated using the quasi-harmonic approximation *via* GIBBS2. For all compositions, the bulk modulus decreases with increasing temperature, reflecting typical lattice softening due to enhanced atomic vibrations. At ambient pressure, bulk moduli are comparatively lower and decrease from Rb_3SbF_6 to Rb_3SbI_6, consistent with the trend of increasing halide ionic radius and weaker lattice cohesion. Under 10 GPa, the bulk moduli are substantially higher, indicating lattice stiffening under compression, while their temperature dependence is notably less steep, suggesting reduced anharmonic effects at high pressure.[35]

Table 5 Computed light yield values for the Rb_3SbX_6 (X = F, Cl, Br, I)[a]

	This work				Other work	
Compounds	Rb_3SbF_6	Rb_3SbCl_6	Rb_3SbBr_6	Rb_3SbI_6	Cs_3SbF_6	Cs_3SbCl_6
LY values (photons per MeV)	73 032.68	95 510.98	112 898.67	140 301.65	106 411.28[A]	123 304.56 (ref. 25)

[a] Ref. 25.

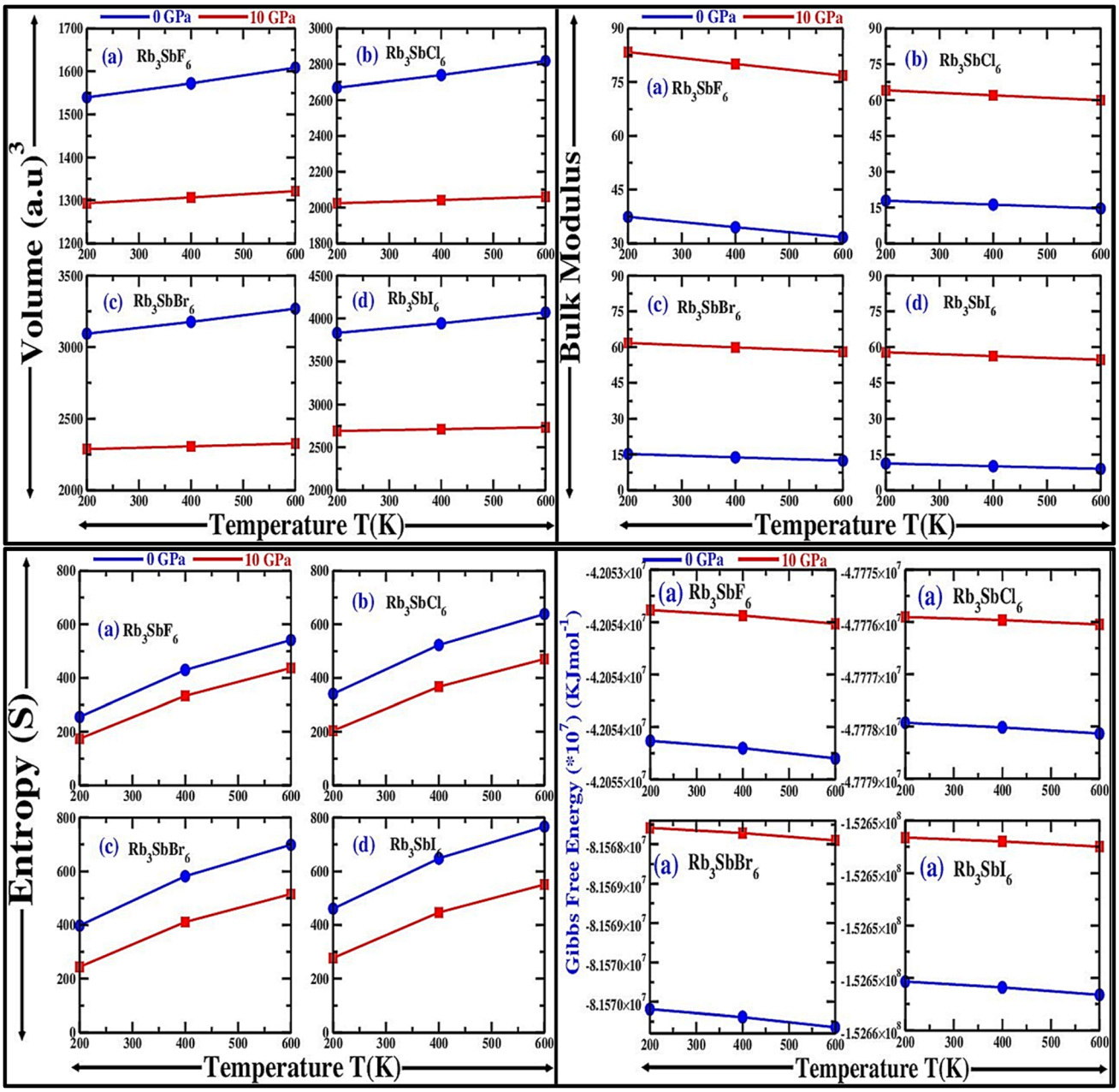

Fig. 6 Computed thermodynamic properties of the Rb_3SbX_6 (a)–(d) (X = F, Cl, Br, I) at (200 to 600) K and (0, and 10) GPa.

Fig. 6 (bottom left) depicts the temperature dependence of entropy for Rb_3SbX_6 (X = F, Cl, Br, I) under pressures of 0 GPa and 10 GPa, highlighting essential thermodynamic characteristics. For all compositions and pressures, entropy increases consistently with temperature. This behavior is attributed to enhanced kinetic energy at elevated temperatures, which allows access to a greater number of microstates, thereby increasing the system's disorder. Conversely, entropy exhibits a clear negative correlation with pressure. At a fixed temperature, increasing the pressure from 0 GPa to 10 GPa results in a reduction of entropy. This effect arises from the material's compression under pressure, which constrains atomic and molecular movement, reduces the available phase space for configurations, and thus lowers overall disorder.[35]

The Gibbs free energy (G), defined by $G = H - TS$ (where H represents enthalpy, T is temperature, and S is entropy), is a crucial parameter for assessing the stability of materials under varying temperature and pressure. For the Rb_3SbX_6 series, analyzing the Gibbs free energy as a function of these variables provides critical insights into their thermal and mechanical stability. Fig. 6 (bottom right) demonstrates that Gibbs free energy decreases with increasing temperature from 200 K to 600 K at both pressure conditions. This trend aligns with theoretical expectations since the entropy term ($-TS$) grows with temperature, reducing the free energy. At 10 GPa, the Gibbs free energy values are slightly less negative than at 0 GPa across all temperatures, indicating a minor reduction in thermodynamic stability under higher pressure. Nevertheless, the small

differences between the two pressure conditions suggest that the Rb_3SbX_6 compounds maintain thermodynamic stability over the entire range of temperatures and pressures examined.[25,35]

4 Conclusion

In this work, the structural, electronic, mechanical, optical, thermodynamic, and scintillation-relevant properties of the lead-free halide double perovskites Rb_3SbX_6 (X = F, Cl, Br, I) were systematically explored using first-principles calculations within the DFT framework. All compounds exhibit wide, direct band gaps, making them suitable for UV photodetectors and high-energy radiation detection. The mechanical analysis confirms the mechanical stability of all phases, with ductile behavior observed in $Rb_3Sb(F/Cl/I)_6$ and brittleness in Rb_3SbBr_6. Optical investigations reveal that halide substitution strongly influences light yield, absorption, and dielectric behavior. Thermodynamic results demonstrate thermal stability across the studied temperature and pressure range, with predictable trends in entropy, Gibbs free energy, and bulk modulus. Among the series, Rb_3SbI_6 emerges as the most promising candidate for optoelectronic and scintillation applications. These findings provide a theoretical basis for further experimental studies and potential device integration of these environmentally friendly, lead-free double perovskites.

Conflicts of interest

The author declares no conflict of interest.

Data availability

The data supporting the findings of this study are available from the corresponding author upon reasonable request. All computational input files, output data, and analysis scripts related to the first-principles calculations of Rb_3SbX_6 (X = F, Cl, Br, I) lead-free mixed-halide double perovskites including structural optimizations, electronic band structure, density of states, phonon dispersion, and optical property simulations have been archived and can be provided for academic and non-commercial research purposes.

Acknowledgements

This research work is supported by the Ministry of Higher Education (MOHE) under the 2023 Translational Research Program for the Energy Sustainability Focus Area (Project ID: MMUE/240001), the 2024 ASEAN IVO (Project ID: 2024-02), and Multimedia University, Malaysia.

References

1 F. Tayari, S. S. Teixeira, M. P. F. Graca and K. I. Nassar, A Comprehensive Review of Recent Advances in Perovskite Materials: Electrical, Dielectric, and Magnetic Properties, *Inorganics*, 2025, **13**, 67.

2 A. Kojima, K. Teshima, Y. Shirai and T. Miyasaka, Organometal Halide Perovskites as Visible-Light Sensitizers for Photovoltaic Cells, *J. Am. Chem. Soc.*, 2009, **131**, 6050–6051.

3 S. Khatoon, S. Kumar Yadav, V. Chakravorty, J. Singh, R. Bahadur Singh, M. S. Hasnain and S. M. M. Hasnain, Perovskite solar cell's efficiency, stability and scalability: A review, *Mater. Sci. Energy Technol.*, 2023, **6**, 437–459.

4 L. Sanga, C. Lalengmawia, Z. Renthlei, S. T. Chanu, L. Hima, N. S. Singh, A. Yvaz, S. Bhattarai and D. P. Rai, A review on perovskite materials for photovoltaic applications, *Next Mater.*, 2025, **7**, 100494.

5 M. Saliba, T. Matsui, J.-Y. Seo, K. Domanski, J.-P. Correa-Baena, M. K. Nazeeruddin, S. M. Zakeeruddin, W. Tress, A. Abate, A. Hagfeldt and M. Grätzel, Cesium-containing triple cation perovskite solar cells: improved stability, reproducibility and high efficiency, *Energy Environ. Sci.*, 2016, **9**, 1989–1997.

6 H. Ahmed, S. Mukhtar, S. Agathopoulos and S. Z. Ilyas, Structural, Electronic, and Optical Properties of Ga-Based Lead-Free Mixed-Halide Perovskites Cs3GaI6-xBrx ($0 \leq x \leq 6$) for Solar Cell Applications: A DFT Study, *Phys. B*, 2022, **640**, 414085.

7 C. N. Jua, M. Vubangsi, E. P. Etape, E. A. Nforna and J. N. Ghogomu, DFT study of the effects of substitution of Pb by Ca, Co and Fe on the structural, electronic and optical properties of methylammonium and formamidinium lead chlorides, *Comput. Condens. Matter.*, 2025, **43**, e01048.

8 G. G. Njema and J. K. Kibet, A review of chalcogenide-based perovskites as the next novel materials: Solar cell and optoelectronic applications, catalysis and future perspectives, *Next Nanotechnol.*, 2025, **7**, 100102.

9 H. Kim, J. S. Han, J. Choi, S. Y. Kim and H. W. Jang, Halide Perovskites for Applications beyond Photovoltaics, *Small Methods*, 2018, **2**, 1700310.

10 V. Chauhan, D. Tripathi, P. Singh, A. Sharma, M. K. Khanna, R. Kumar, R. Bhatnagar and T. Kumar, Prospects for lead free perovskite for photovoltaic applications and biological impacts: Challenges and opportunities, *Inorg. Chem. Commun.*, 2023, **157**, 111421.

11 C. C. Li, T. Yu Huang, Y. H. Lai, Y. C. Huang and C. Shan Tan, Lead-free perovskites for flexible optoelectronics, *Mater. Today Electron.*, 2024, **8**, 100095.

12 G. Volonakis, M. R. Filip, A. A. Haghighirad, N. Sakai, B. Wenger, H. J. Snaith and F. Giustino, Lead-Free Halide Double Perovskites via Heterovalent Substitution of Noble Metals, *J. Phys. Chem. Lett.*, 2016, **7**, 1254–1259.

13 S. Murugan and E.-C. Lee, Recent Advances in the Synthesis and Application of Vacancy-Ordered Halide Double Perovskite Materials for Solar Cells: A Promising Alternative to Lead-Based Perovskites, *Materials*, 2023, **16**, 5275.

14 I. H. Al-Lehyani, A first-principle study of the stability and electronic properties of halide inorganic double perovskite Cs2PbX6 (X = Cl,I) for solar cell application, *Arab. J. Chem.*, 2021, **14**, 102920.

15 M. T. Klug, A. Osherov, A. A. Haghighirad, S. D. Stranks, P. R. Brown, S. Bai, J. T.-W. Wang, X. Dang, V. Bulović, H. J. Snaith and A. M. Belcher, Tailoring metal halide perovskites through metal substitution: influence on photovoltaic and material properties, *Energy Environ. Sci.*, 2017, **10**, 236–246.

16 Y.-X. Li, J. Zhong, X.-J. Xiong, Y.-Q. Ning, Y. Xu, H.-P. Zhu, Y.-Q. Zhao and B. Li, Optoelectronic and transport properties of layer-dependent two-dimensional perovskite Cs3Bi2I9, *Phys. Lett. A*, 2024, **528**, 130053.

17 S. L. Hamukwaya, H. Hao, M. M. Mashingaidze, T. Zhong, S. Tang, J. Dong, J. Xing and H. Liu, Potassium Iodide-Modified Lead-Free Cs3Bi2I9 Perovskites for Enhanced High-Efficiency Solar Cells, *Nanomaterials*, 2022, **12**, 3751.

18 S. Li, S. Song, P. Lv, S. Wang, J. Hong and G. Tang, Enhanced charge transport in A-site ordered perovskite derivatives $A_2A'Bi_2I_9$ (A = Cs; A′ = Ag, Cu): a first-principles study, *Phys. Chem. Chem. Phys.*, 2025, **27**, 14948–14956.

19 S. Ghorui, J. Kangsabanik, M. Aslam and A. Alam, Optoelectronic and transport properties of vacancy-ordered double-perovskite halides: A first-principles study, *Phys. Rev. Appl.*, 2024, **21**, 024036.

20 H. I. Ali, A. Ayyaz, N. D. Alkhaldi, I. Boukhris, M. S. Al-Buriahi, Q. Mahmood, T. Alshahrani and S. Bouzgarrou, Forecasting phase stability, optoelectronic behavior, and transport mechanisms of double perovskites Cs2AuMX6 (M = As, Bi and X = Cl, Br) for applications in renewable energy technologies, *Inorg. Chem. Commun.*, 2025, **176**, 114301.

21 M. Saiduzzaman, T. Ahmed, K. M. Hossain, A. Biswas, S. K. Mitro, A. Sultana, M. S. Alam and S. Ahmad, Band gap tuning of non-toxic Sr-based perovskites CsSrX3 (X = Cl, Br) under pressure for improved optoelectronic applications, *Mater. Today Commun.*, 2023, **34**, 105188.

22 Y.-T. Huang, S. R. Kavanagh, D. O. Scanlon, A. Walsh and R. L. Z. Hoye, Perovskite-inspired materials for photovoltaics and beyond—from design to devices, *Nanotechnology*, 2021, **32**, 132004.

23 G. Laurita and R. Seshadri, Chemistry, Structure, and Function of Lone Pairs in Extended Solids, *Acc. Chem. Res.*, 2022, **55**, 1004–1014.

24 S. Adhikari and P. Johari, Theoretical insights into monovalent-metal-cation transmutation effects on lead-free halide double perovskites for optoelectronic applications, *Phys. Rev. Mater.*, 2023, **7**, 075401.

25 M. Y. Khan, M. A. Jehangir, N. Israr, A. Hassan, U. Younis, J. Khan, M. Khan, A. Khan and A. Al Souwaileh, First-principles study of Cs3SbX6 (X = F, Cl) for scintillation and optoelectronic applications, *Phys. B*, 2025, **707**, 417150.

26 M. A. Javed, R. Ahmed, S. A. Tahir and B. Ul Haq, Investigations of optoelectronic and scintillating properties of novel halide perovskites Cs2KSnX6 (X=Cl, Br, I), *J. Solid State Chem.*, 2025, **341**, 125084.

27 M. A. Jehangir, G. Murtaza, A. R. Chaudhry, K. Ali Khan, M. D. Albaqami, N. Israr, S. H. Shah and M. Ibrar, Optical and Transport Properties of Novel X2bagcl6 (Where K, Rb, Cs, and B = Sc, Y) Double Pervoskites, *SSRN*, 2024, DOI: 10.2139/ssrn.4844866.

28 M. Manzoor, J. A. Abraham, R. Sharma, M. Aslam, A. Kumar, F. N. Almutairi, M. Jeridi and H. Ullah, Probing the Optoelectronic and Thermoelectric Performance of Inorganic Halide Perovskite Rb2KInI6 for Renewable Energy Applications via DFT Computations, *J. Inorg. Organomet. Polym.*, 2025, **35**, 3296–3312.

29 M. Born, On the stability of crystal lattices. I, *Math. Proc. Camb. Phil. Soc.*, 1940, **36**, 160–172.

30 N. Israr, M. A. Jehangir, A. M. Tighezza, S. Khan, G. Murtaza and M. Saeed, The effect of PBEsol GGA and mBJ potentials on the structural, electronic, optical, elastic and thermoelectric properties of A2BAuI6 (A = K or Rb or Cs, B = Sc or Y), *Mater. Sci. Semicond. Process.*, 2025, **186**, 109116.

31 M. A. Jehangir, G. Murtaza, M. D. Albaqami, S. Mohammad, S. Khan, N. Israr, M. Shafiq and S. H. Shah, Exploring the stability, optoelectronic, and thermoelectric properties of Sc-based double perovskites X_2ScAgI_6 (X = K, Rb, Cs) for renewable energy applications, *Comput. Condens. Matter.*, 2025, **42**, e00988.

32 U.-G. Jong, C.-J. Yu and Y.-H. Kye, Computational prediction of structural, electronic, and optical properties and phase stability of double perovskites K_2SnX_6 (X = I, Br, Cl), *RSC Adv.*, 2020, **10**, 201–209.

33 V. B. Bobrov, S. A. Trigger, G. J. F. Van Heijst and P. P. J. M. Schram, Kramers-Kronig relations for the dielectric function and the static conductivity of Coulomb systems, *Europhys. Lett.*, 2010, **90**, 10003.

34 A. Otero-de-la-Roza, D. Abbasi-Pérez and V. Luaña, Gibbs2: A new version of the quasiharmonic model code. II. Models for solid-state thermodynamics, features and implementation, *Comput. Phys. Commun.*, 2011, **182**, 2232–2248.

35 K. Deepthi Jayan and V. Sebastian, Ab initio DFT determination of structural, mechanical, optoelectronic, thermoelectric and thermodynamic properties of RbGeI3 inorganic perovskite for different exchange-correlation functionals, *Mater. Today Commun.*, 2021, **28**, 102650.

36 I. A. Shah, M. Imran, N. A. Niaz, F. Hussain, U. Rasheed, M. Alam, S. M. Ali, R. M. A. Khalil and M. Shoaib, Revealing structural, elastic, optoelectronic and thermoelectric properties of lead-free Ba2XTiO6 (X = Hf, Ce, Te) double perovskite for solar cells applications, *J. Comput. Electron.*, 2024, **23**, 396–406.

37 S. Hussain and J. U. Rehman, First-principles calculation to investigate structural, electronic, optical, and thermodynamics properties of perovskite KXO3 (K Ta and Zn) alloys for photovoltaic and smart window applications, *Phys. B*, 2024, **687**, 416116.

38 C. J. Bartel, C. Sutton, B. R. Goldsmith, R. Ouyang, C. B. Musgrave, L. M. Ghiringhelli and M. Scheffler, New tolerance factor to predict the stability of perovskite oxides and halides, *Sci. Adv.*, 2019, **5**, eaav0693.

39 A. Ayyaz, G. Murtaza, A. Usman, N. Sfina, A. S. Alshomrany, S. Younus and S. Saleem, Urwa-tul-Aysha, Evaluation of Physical Properties of A2ScCuCl6 (A = K, Rb, and Cs)

Double Perovskites via DFT Framework, *J. Inorg. Organomet. Polym.*, 2024, **34**, 3560–3575.

40 A. K. Datta, M. K. Hossain, Md. S. Rahman, P. Paramasivam, A. El-marghany and V. K. Mishra, DFT insights into bandgap engineering of lead-free LiMCl3 (M = Mg, Be) halide perovskites for optoelectronic device applications, *Sci. Rep.*, 2025, **15**, 6944.

41 N. Rahman, M. Husain, V. Tirth, A. Algahtani, H. Alqahtani, T. Al-Mughanam, A. H. Alghtani, R. Khan, M. Sohail, A. A. Khan, A. Azzouz-Rached and A. Khan, Appealing perspectives of the structural, electronic, elastic and optical properties of $LiRCl_3$ (R = Be and Mg) halide perovskites: a DFT study, *RSC Adv.*, 2023, **13**, 18934–18945.

42 A. Boutramine, S. Al-Qaisi, S. Samah, A. K. Alqorashi, T. A. Alrebdi, M. Ezzeldien and Md. F. Rahman, First-principles Investigations of Structural, Thermodynamic, Optoelectronic and Thermoelectric Properties of Rb2CuMF6 (M = As3+, Bi3+) Eco-friendly Halide Double Perovskites: Materials for Green Energy Applications, *J. Inorg. Organomet. Polym.*, 2024, **34**, 4374–4391.

43 A. Ayyaz, M. Zaman, H. D. Alkhaldi, H. I. Ali, I. Boukhris, S. Bouzgarrou, M. M. Al-Anazy and Q. Mahmood, Computational screening of appealing perspectives of indium-based halide double perovskites In_2 $AgSbX_6$ (X = Cl, Br, and I) for energy harvesting technologies, *RSC Adv.*, 2025, **15**, 11128–11145.

44 Z. Jin, Y. Wu, S. Li, Q. Wu, S. Chen, Y. Chen, W. Zhang and C. Zhang, Electronic structure, elastic, optical and thermodynamic properties of cubic perovskite NaBaF3 with pressure effects: First-principles calculations, *Results Phys.*, 2021, **22**, 103860.

45 N. Israr, S. Khan, A. El-marghany, M. A. Jehangir, S. Shakeel and G. Murtaza, Exploring the Structural, Mechanical and Optical Properties of K2InGaX6 (X = Cl, Br or I) Compounds by Density Functional Theory, *J. Inorg. Organomet. Polym.*, 2025, DOI: **10.1007/s10904-025-03731-6**.

46 N. Rahman, M. Husain, J. Yang, M. Sajjad, G. Murtaza, M. Ul Haq, A. Habib, Zulfiqar, A. Rauf, A. Karim, M. Nisar, M. Yaqoob and A. Khan, First principle study of structural, electronic, optical and mechanical properties of cubic fluoro-perovskites: (CdXF3, X = Y, Bi), *Eur. Phys. J. Plus*, 2021, **136**(3), 347.

47 M. Jamil, Q. Ain, J. Munir, H. Murtaza, H. M. Ghaithan, A. S. Aldwayyan, A. A. A. Ahmed and S. M. H. Qaid, Investigations of the Structural, Mechanical and Optoelectronic Attributes of Rb2TlB′I6 (B′ = As, Ga) Double Perovskites for Photovoltaics, *J. Inorg. Organomet. Polym.*, 2024, **34**, 3984–3994.

48 J. Yang, L.-Y. Fu, B.-Y. Fu, Z. Wang and W. Hou, High-temperature effect on the material constants and elastic moduli for solid rocks, *J. Geophys. Eng.*, 2021, **18**, 583–593.

49 M. E. Fine, L. D. Brown and H. L. Marcus, Elastic constants versus melting temperature in metals, *Scripta Metall.*, 1984, **18**, 951–956.

50 S. Hussain, S. Aftab, H. Muneer, M. U. Ghani, J. U. Rehman and M. B. Tahir, Study of ultra-wide bandgap beryllium based perovskite ZBeF3 (Z = Na, Rb, Cs) alloys for smart window applications: A DFT insights, *Comput. Condens. Matter.*, 2024, **41**, e00958.

51 U. Ayaz, A. Shazia, M. Husain, N. Rahman and E. Bonyah, *Ab initio* investigation of structural, electronic, magnetic, elastic, and optical properties of Cs-based chloro-perovskites CsXCl3 (X = Be and Rh), *AIP Adv.*, 2021, **11**, 105215.

52 N. Erum and J. Ahmad, Structural, Elastic and Mechanical Properties of Cubic RbMF3 (V, Mn, Fe, Co, Ni, Cu, and Zn) Perovskite Materials, *Arch. Adv. Eng. Sci.*, 2023, **2**, 24–29.

53 A. Raza, A. Afaq, M. S. Kiani, M. Ahmed, A. Bakar and M. Asif, First-principles calculations to investigate elasto-mechanical and opto-electronic properties of pyrochlore oxides X2Zr2O7 (X=La, Nd), *J. Mater. Res. Technol.*, 2022, **18**, 5005–5018.

54 D.-M. Han, X.-J. Liu, S.-H. Lv, H.-P. Li and J. Meng, Elastic properties of cubic perovskite BaRuO3 from first-principles calculations, *Phys. B*, 2010, **405**, 3117–3119.

55 M. Ibrar, G. Murtaza, M. Haneef, M. A. Jehangir, N. H. Alotaibi, S. Mohammad, B. Bashir and T. Zaman, Elastic-acoustic, optical and thermoelectric investigation of Cu6AsS5X (X= Br, I) for renewable energy applications, *Comput. Condens. Matter.*, 2024, **40**, e00946.

56 M. I. Naher and S. H. Naqib, An ab-initio study on structural, elastic, electronic, bonding, thermal, and optical properties of topological Weyl semimetal TaX (X = P, As), *Sci. Rep.*, 2021, **11**, 5592.

57 R. Ahmed, M. Mahamudujjaman, M. A. Afzal, M. S. Islam, R. S. Islam and S. H. Naqib, DFT based comparative analysis of the physical properties of some binary transition metal carbides XC (X = Nb, Ta, Ti), *J. Mater. Res. Technol.*, 2023, **24**, 4808–4832.

58 R. Gaillac, P. Pullumbi and F.-X. Coudert, ELATE: an open-source online application for analysis and visualization of elastic tensors, *J. Phys.: Condens. Matter*, 2016, **28**, 275201.

59 M. Q. Shah, M. Shafiq, A. Naeem, G. Murtaza, A. Ayyaz, A. Usman, S. M. Deen and M. A. El-Sheikh, Effect of position occupancy of different elements on the structural stability, optoelectronic, thermoelectric and elastic properties of Cs2CuAsX6 (X: Cl, Br, I) halide double perovskite: DFT analysis, *Mater. Sci. Semicond. Process.*, 2024, **174**, 108187.

60 L. J. Wang, A. Kuzmich and A. Dogariu, correction: Gain-assisted superluminal light propagation, *Nature*, 2001, **411**, 974.

61 M. Saeed, M. A. Jehangir, G. Murtaza, A. R. Chaudhry, K. A. Khan, M. D. Albaqami, N. Israr, S. H. Shah and M. Ibrar, Optical and transport properties of novel X2BAgCl6 (where X = K, Rb, Cs, and B = Sc, Y) double perovskites, *Mater. Sci. Eng., B*, 2024, **308**, 117556.

62 N. Israr, F. Alresheedi, M. Saeed, A. Rasool Chaudhry, M. Awais Jehangir and G. Murtaza, First-principles calculations to investigate Electronic, Optical, Mechanical, and transport characteristics of novel A2BAuCl6 (A = K/Rb/Cs; B = Sc/Y), *Results Phys.*, 2024, **66**, 108017.

63 N. Israr, W. U. Rehman, M. A. Jehangir, N. S. A. EL-Gawaad and U. Farooq, First-Principles Investigation of Narrow Bandgap Halide Double Perovskites A2AgSbI6 (A = K, Rb),

J. Inorg. Organomet. Polym., 2025, DOI: 10.1007/s10904-025-03695-7.

64 A. A. Khan, A. U. Rehman, A. Laref, M. Yousaf and G. Murtaza, Structural, Optoelectronic and Thermoelectric Properties of Ternary $CaBe_2$ X_2 (X = N, P, As, Sb, Bi) Compounds, *Z. Naturforsch. A*, 2018, **73**, 965–973.

65 Q. Mahmood, M. Hassan, K. C. Bhamu, M. Yaseen, S. M. Ramay and A. Mahmood, Density functional theory-based study of the magnetic and optical properties of PbMO3 (M = Cr, Fe) using the modified BeckeJohnson mBJ functional, *J. Phys. Chem. Solids*, 2019, **128**, 275–282.

66 M. A. Blanco, E. Francisco and V. Luaña, GIBBS: isothermal-isobaric thermodynamics of solids from energy curves using a quasi-harmonic Debye model, *Comput. Phys. Commun.*, 2004, **158**, 57–72.